Commun. Comput. Phys.
doi: 10.4208/cicp.060709.060110a

Vol. **8**, No. 2, pp. 265-288
August 2010

A Level Set Immersed Boundary Method for Water Entry and Exit

Yali Zhang[1,*], Qingping Zou[1], Deborah Greaves[1], Dominic Reeve[1],
Alison Hunt-Raby[1], David Graham[2], Phil James[2] and Xin Lv[1]

[1] *School of Marine Science and Engineering, University of Plymouth, United Kingdom, PL4 8AA.*
[2] *School of Mathematics and Statistics, University of Plymouth, United Kingdom, PL4 8AA.*

Received 6 July 2009; Accepted (in revised version) 6 January 2010

Communicated by Boo Cheong Khoo

Abstract. The interaction between free surface flow and structure is investigated using a new level set immersed boundary method. The incorporation of an improved immersed boundary method with a free surface capture scheme implemented in a Navier-Stokes solver allows the interaction between fluid flow with free surface and moving body/bodies of almost arbitrary shape to be modelled. A new algorithm is proposed to locate exact forcing points near solid boundaries, which provides an accurate numerical solution. The discretized linear system of the Poisson pressure equation is solved using the Generalized Minimum Residual (GMRES) method with incomplete LU preconditioning. Uniform flow past a cylinder at Reynolds number Re=100 is modelled using the present model and results agree well with the experiment and numerical data in the literature. Water exit and entry of a cylinder at the prescribed velocity is also investigated. The predicted slamming coefficient is in good agreement with experimental data and previous numerical simulations using a ComFlow model. The vertical slamming force and pressure distribution for the free falling wedge is also studied by the present model and comparisons with available theoretical solutions and experimental data are made.

AMS subject classifications: 6D05, 76T10, 65B99, 65E05

Key words: Level set method, immersed boundary method, slamming coefficient, water entry and exit, free surface, fluid-structure interaction.

---

[*] Corresponding author. *Email addresses:* `yali.zhang@plymouth.ac.uk` (Y. Zhang), `qingping.zou@plymouth.ac.uk` (Q. Zou), `deborah.greaves@plymouth.ac.uk` (D. Greaves), `dominic.reeve@plymouth.ac.uk` (D. Reeve), `alison.hunt-raby@plymouth.ac.uk` (A. Hunt-Raby), `david.graham@plymouth.ac.uk` (D. Graham), `phil.james@plymouth.ac.uk` (P. James), `xin.lv@plymouth.ac.uk` (X. Lv)

1 Introduction

Investigation of fluid structure interaction at the free surface is a classical hydrodynamic problem and has a wide range of applications particularly in the fields of naval architecture, civil and ocean engineering and physical oceanography. A flow singularity occurs when a body impacts the free surface, which gives rise to a high pressure peak localized at the spray root and makes water entry and exit problems difficult. In grid based numerical methods, there are two main strategies to handle a moving or deforming boundary problem with topological change, namely body conforming moving grids (Baum et al. 1996; Yan et al. 2007) and embedded fixed grids (Yang et al. 1997; Ye et al. 1999; Tucker et al. 2000; Fadlun et al. 2000; Tseng et al. 2003; Balaras et al. 2004; Yang et al. 2006; Lv et al., 2006). For the former method, the grid can be efficiently deformed in an arbitrary Lagrangean-Eulerian (ALE) frame of reference to minimize distortion if the geometric variation is quite modest. Boundary conditions can be applied at the exact location of the rigid boundary. However, if the change of topology is complex, it will be very difficult and time consuming to regenerate the mesh. Also difficulties arise in the form of grid skewness and additional numerical dissipation may be a consequence of the redistribution of the field variables in the vicinity of the boundary.

An alternative to body conforming moving grids is embedded fixed grids where the governing equations are usually discretized on fixed Cartesian grids. The method can also be divided into two major classes based on the specific treatment of the boundary cells; (1) Cartesian cut cell methods (Yang et al. 1997; Ye et al. 1999; Tucker et al. 2000) and (2) Immersed boundary methods (Fadlun et al. 2000; Tseng et al. 2003; Balaras et al. 2004; Yang et al. 2006; Lv et al., 2006). Although the Cartesian cut cell method was originally developed for potential flow, it has been applied and extended to the Euler equations, shallow water equations, Navier-Stokes equations to simulate low speed incompressible flows and flows with moving interfaces. It has the potential to significantly simplify and automate the difficulty of mesh generation. There are also a number of disadvantages inherent in the use of this method. It cuts the solid body out of a background Cartesian mesh, which can generate sharp corners and a variety of different cut cell types. Thus, extending this method to three-dimensions is not a trivial task. In addition, arbitrarily small cells arising near solid boundaries due to the Cartesian mesh intersecting a solid body can restrict the stability of the Cartesian solvers.

In the immersed boundary method the momentum forcing which is introduced to enforce the boundary condition of the body in the fluid can be prescribed on a fixed mesh so that the accuracy and efficiency of the solution procedure on simple grids is maintained. Bodies of almost arbitrary shape can be dealt with and flows with multiple bodies or islands can be computed at reasonable computational cost (Fadlun et al. 2000). The immersed boundary method has the advantage of simplified grid generation and inherent simplicity which allows the study of moving bodies (Mittal et al. 2005) on fixed Cartesian grids. Furthermore, the appropriate treatment in the immersed boundary method leads to a convenient method for computing forces acting on a body, namely lift and drag forces. These advantages suggest that it is well suited to study problems involving a moving body with the free surface flow.

The work here builds on earlier work by Zhang et al. (2009) in which a level set method with global mass correction was developed for two fluid flows and applied to simulate water column collapse and free surface waves over a submerged structure. A major contribution of the present work is the incorporation of an improved immersed boundary method with the free surface model. This makes it straightforward to undertake a variety of fluid structure interaction problems. A new algorithm is proposed to locate exact forcing points near the solid boundaries, which provides an accurate numerical solution. To accelerate the convergence of the solution of the Poisson pressure equation the Generalized Minimum Residual (GMRES) method with incomplete LU factorization for preconditioning is applied. This paper is organized as follows. First, governing equations are discussed in Section 2. Then numerical methodologies for the Navier-Stokes, free surface and immersed boundary method are described in Section 3. The problems arising from the classification of the grid points, direct forcing for the forcing points, hydrodynamic forces on the body and interaction between the fluid and structure are also discussed in this section in detail. Results are presented in Section 4; initially uniform flow over a circular cylinder at $\mathrm{Re}=100$ is simulated to demonstrate the accuracy of the present level set immersed boundary method. Next, it is used to calculate water exit and entry of a cylinder. Snapshots of the simulations have been compared with photographs of experiments by Greenhow et al. (1983). The slamming coefficients of water entry of a cylinder are compared to the theory, experiment and ComFlow (Kleefsman et al. 2005). Results of a free falling wedge where a full coupling between the fluid and body are presented and compared with experimental results and previous numerical simulations in the literature. Conclusions and future work are given in Section 5.

2 Governing equations

2.1 Navier-Stokes equations

The governing equations for an incompressible fluid flow are the mass conservation equation and the Navier-Stokes momentum conservation equations written as

$$\frac{\partial u_i}{\partial x_i}=0, \tag{2.1}$$

and

$$\frac{\partial u_i}{\partial t}+\frac{\partial\left(u_iu_j\right)}{\partial x_j}=-\frac{1}{\rho}\frac{\partial p}{\partial x_i}+\frac{1}{\rho}\frac{\partial \tau_{ij}}{\partial x_j}+f_i, \tag{2.2}$$

where Cartesian tensor notation is used, $(i=1,2)$, u_j, p and x_j are the velocities, pressure and spatial coordinates respectively, f_i represents momentum forcing components. τ_{ij} is the viscous term given by

$$\tau_{ij}=\mu\left(\frac{\partial u_i}{\partial x_j}+\frac{\partial u_j}{\partial x_i}\right), \tag{2.3}$$

where ρ and τ are the density and viscosity respectively appropriate for the phase that is occupying the particular spatial location at a given instant.

2.2 Free surface equations

Due to the existence of steep gradients in density and viscosity across the free surface, excessive numerical diffusion is experienced when computing viscous flows (Ferziger, 2002; Wang, et al. 2009). Here, the level set method is used to capture the interface between the two phases. The evolution of the level-set function, ϕ, is governed by

$$\frac{\partial\phi}{\partial t}+u_j\frac{\partial\phi}{\partial x_j}=0. \tag{2.4}$$

The solution of the Navier-Stokes equations will yield unwanted instabilities at the interface if density and viscosity are discontinuous there. To overcome this, a region of finite thickness over which a smooth but rapid change of density and viscosity occurs across the interface is introduced. This is achieved by defining a smoothed Heaviside function.

$$H(\phi)=\begin{cases} 0, & \phi<-\varepsilon, \\ \dfrac{\phi+\varepsilon}{2\varepsilon}+\dfrac{1}{2\pi}\sin\left(\dfrac{\pi\phi}{\varepsilon}\right), & -\varepsilon\leqslant\phi\leqslant\varepsilon, \\ 1, & \phi>\varepsilon, \end{cases} \tag{2.5}$$

where ε is related to the grid size. Using the smoothed Heaviside function, these properties are calculated using

$$\beta=(1-H)\beta_1+H\beta_2, \tag{2.6}$$

where β can be density, viscosity or another property of interest. Since ϕ is the signed normal distance from the interface, it satisfies

$$\nabla|\phi|=0. \tag{2.7}$$

When Eq. (2.4) moves the level set $\phi=0$ at the correct velocity, ϕ may become irregular after some period of time (Sussman et al. 1994) and its properties as a distance function may be lost. Thus, to ensure that ϕ remains a distance function that satisfies Eq. (2.4), redistancing must be performed. This is achieved by solving for a second distance function ϕ' given by Eq. (2.8):

$$\frac{\partial\phi'}{\partial\bar{t}}+s(\phi)\left(\left|\nabla\phi'\right|-1\right)=0. \tag{2.8}$$

Here, $\bar{t}$ is a pseudo time for the variable ϕ', the initial condition is $\phi'(\vec{x},0)=\phi(\vec{x})$ and $s(\phi)$ is the smoothed sign function defined as

$$s(\phi)=\frac{\phi}{\sqrt{\phi^2+(|\nabla\phi|\varepsilon)^2}}. \tag{2.9}$$

For incompressible flows, the total mass is conserved in time. However, the numerical discretization of the level set formulation does not preserve this property in general. Even with the above redistancing process for the level set function, it has been found that a considerable amount of total mass is lost in time (Chang et al. 1996; Yap et al. 2006). To overcome this difficulty, the global mass correction coupled with the first and second distance functions is used to preserve the total mass in time. The steady state solution to a third distance function ϕ'' is obtained using Eq. (2.10):

$$\frac{\partial\phi''}{\partial t'}=M_{cor}, \tag{2.10}$$

where t' and M_{cor} are respectively a pseudo-time, which can be different from $\bar{t}$, and mass correction factor. The steady state values of the second distance function ϕ' are used as the initial condition for Eq. (2.10).

Mass must be removed or added to ensure the conservation of the reference phase. Thus, a dimensionless mass correction term is introduced given by

$$M_{cor}=sign(\phi_{ref})\frac{M_o-M_t}{M_o}, \tag{2.11}$$

where M_o and M_t are the original mass and the mass of the reference phase at time t, respectively. Either fluid can be chosen as the reference fluid. The original mass is the mass calculated at the beginning. The mass at time t increases when there is an injection of the reference phase but decreases when there is removal of the reference phase. Depending on the choice of the reference phase, the mass of the reference can be calculated using

$$M=\begin{cases} \sum\rho_{ref}H_{ref}\Delta V, & H_{ref}=1,\\ \sum\rho_{ref}(1-H_{ref})\Delta V, & H_{ref}=0, \end{cases} \tag{2.12}$$

where ΔV is the area that is occupied by the reference phase.

3 Numerical method

3.1 Navier-Stokes solver

A staggered grid is adopted to ensure strong pressure velocity coupling and to enforce mass conservation in each control volume. The governing Eqs. (2.1) and (2.2) are discretized using a fractional step method.

$$\frac{\tilde{u}_i-u_i^k}{\Delta t}=-\frac{\partial\left(u_i^k u_j^k\right)}{\partial x_j}+\frac{1}{\rho}\frac{\partial \tau_{ij}^k}{\partial x_j}+g_i+f_i^k, \tag{3.1}$$

$$\frac{\partial}{\partial x_i}\left(\frac{1}{\rho}\frac{\partial p}{\partial x_i}\right)=\frac{1}{\Delta t}\frac{\partial \tilde{u}_i}{\partial x_i}, \tag{3.2}$$

$$u_i^{k+1}=\tilde{u}_i-\frac{\Delta t}{\rho}\frac{\partial p}{\partial x_i}, \tag{3.3}$$

where $\tilde{u}_i$ is the intermediate velocity. f_i^k is the momentum forcing used to enforce the desired boundary conditions on an immersed boundary interface and Δt is the time step. The QUICK scheme with deferred correction (Waterson et al. 2007) is used to discretize the convection terms. The viscous terms in Eq. (3.1) are discretized with a second order central difference scheme. When complex geometries are simulated using the immersed boundary method, the convergence is slowed further because the immersed boundaries modify the linear system (Tseng et al. 2003). Therefore, it is desirable to speed up the convergence. In this work, the Generalized Minimum Residual (GMRES) method with incomplete LU factorization for preconditioning (Yousef et al. 1986) is applied to solve the discretized linear system of the Poisson pressure equation.

3.2 Free surface solver

The level set with global mass correction method by Zhang et al. (2009) is used to simulate the free surface. The level set equation is solved using third order ENO for convection terms and a five stage Runge-Kutta scheme for time advancement. The redistancing equation is solved using a similar equation to that given by Sussman et al. (1994). Global mass correction is solved using dual time stepping with a five stage Runge-Kutta.

3.3 Immersed boundary treatment

3.3.1 Classification of computational grids

It is worth pointing out that our method for classifying the fluid points differs from that of Ye et al. (1999) and Balaras (2004). Their methods cause some fluid points or solid points to become forcing points in some topological shapes thus leading to calculation error. Therefore, a method is proposed here to locate exact forcing points.

The interface is described by interfacial markers using the arc length coordinates $\mathbf{X}(s)$ as shown in Fig. 1. The markers are equally spaced on the immersed boundary interface and the spacing is approximately equal to the local grid spacing. The functions $x(s)=a_x s^2+b_x s+c_x$ and $y(s)=a_y s^2+b_y s+c_y$ are generated. The coefficients, a_x, b_x, c_x, a_y, b_y and c_y, are obtained by fitting quadratic polynomials to particle i and its two neighbours $i-1$ and $i+1$. Thus, the normal of a marker to the interface is obtained.

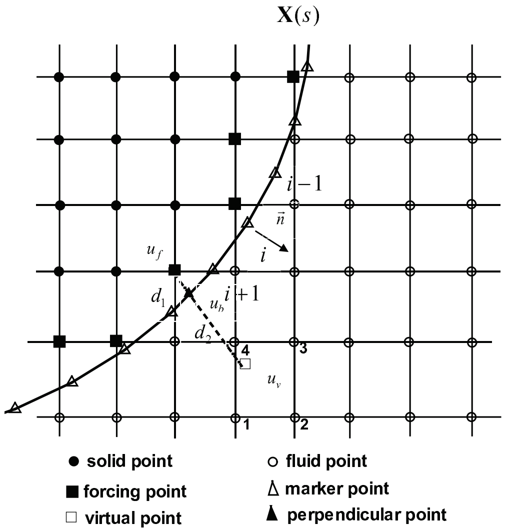

Figure 1: Grid classification and interpolation procedures for the forcing points, u_f.

In order to locate the forcing points accurately, the immersed object is meshed with a triangular grid so that bodies of almost arbitrary shape can be dealt with and flows with multiple bodies or islands can be modelled with no difficulty. Before the identifying process begins, the bounding box that might contain the immersed object is defined around the object by the extrema of the object mesh coordinates to improve the efficiency of the algorithm. Only those fluid grids falling into this box will be checked. Then a do-loop based on the number of the cells in the immersed object triangular mesh is performed. During each cycle of this loop, fluid nodes in the bounding box are tested one by one to see if they fall into a certain cell of the object mesh. There are two vectors defined as shown in Fig. 2: i) The unit normal vectors oriented inward from the triangular face, $\vec{n}$; ii) and the vector $\vec{p}$ pointing from the centre of the triangular face of the cell to the node to be tested. The dot product between these two vectors, $(p_n)^{nedge}$, must be greater than or equal to zero if the angle, θ, subtended between them is less than 90° and less than zero if the angle is greater than 90°.

$$(p_n)^{nedge} = \{\vec{p}\}.\{\vec{n}\} = \{p_x p_y\}.\left\{\begin{array}{c} n_x \\ n_y \end{array}\right\} = \left(p_x n_x + p_y n_y\right)^{nedge}, \quad nedge = 1 \text{ to } 3, \tag{3.4}$$

where the superscript "nedge" is the triangular edge number of the triangular cell.

With reference to Fig. 2(a), for the 2D case, the dot product between these two vectors must be positive for the three edges if the suspected node is to fall within the structure cell. If one of the dot products between these two vectors is less than zero, then the node being tested is not within the cell, as depicted in Fig. 2(b). In order to reduce the preprocessing CPU time further, those nodes that fall within a particular cell are marked

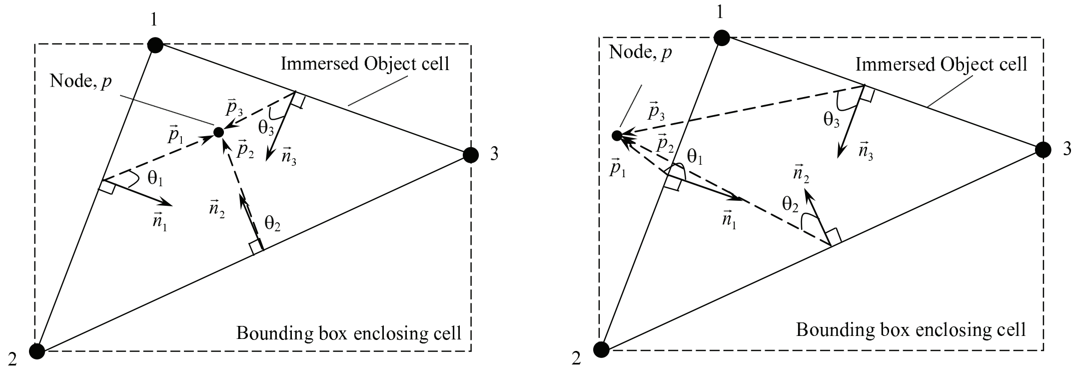

(a) (b)

Figure 2: Two scenarios of testing process for the classification of the computational grids.

with flag 0 and will not be tested further. The forcing points as identified in Fig. 1, which are points with flag -1 in the solid phase with at least one neighbouring point in the fluid. Thus all Eulerian grid points are divided into three categories: (1) forcing points, which are grid points with flag -1 in the solid phase that have one or more neighbouring points in the fluid phase; (2) fluid points, which are all the points with flag 0 in the fluid phase; (3) solid points, which are all the remaining points with flag 1 in the solid phase. Ye et al. (1993) used the reshaped cell method and Yang et al. (2006) applied the field-extension to treat the points of moving boundaries in the fluid. In this study the ghost node rather than the reshaped cell and field extension method is used to enforce the boundary condition. This can greatly simplify the numerical implementation and save CPU time by reducing an additional field-extension or reshaped cell step. Moreover, the internal treatment is not necessary with the present method while it is required in the spectral simulations of Goldstein et al. (1993) near the immersed boundary.

3.3.2 Momentum forcing and interpolation for the velocity

When Eq. (2.2) is discretized explicitly in time, the discrete form can be written as (Tseng et al. 2003; Balaras 2004)

$$\frac{u_i^{k+1}-u_i^k}{\Delta t}=\mathrm{RHS}_i^k+f_i^k, \tag{3.5}$$

where Δt is the time step and RHS_i^k includes the convective, viscous, pressure gradient and body force of the governing equations. If the forcing f_i^k must yield $u_i^{k+1}=u_b$ on the immersed boundary where u_b is the Dirichlet boundary condition at the immersed boundary, the forcing is given from the above equation.

$$f_i^k=\frac{u_b-u_i^k}{\Delta t}-\mathrm{RHS}_i^k. \tag{3.6}$$

This forcing is direct in the sense that the desired boundary condition can be satisfied at every time step. Evaluating the force f_i^k requires no additional CPU time since it does not involve the computation of extra terms. Furthermore it does not influence the stability of the time advancement scheme. Although the basic idea is demonstrated, Eulerian grid nodes almost never coincide with the immersed boundary in practical applications. Thus, f_i^k needs to be computed at grid points near and not exactly on the interface.

The value, u_f, at the forcing points in Fig. 1 is not known and has to be reconstructed using the information from the interface and surrounding field. First a virtual point, u_v, of the forcing point, u_f, is located along the normal to the boundary. The location of the virtual point on the line normal to the boundary is determined in such a way that $d_1=d_2$, where d_1 is the distance between the forcing point and perpendicular point, u_b, and d_2 is the distance between the perpendicular point and virtual point. If any of the points in the stencil 1-4 is a forcing point, the virtual point is relocated in a way such that $d_2>d_1$. This can be done by increasing the initial distance by one grid distance. Then the value of the virtual point u_v can be interpolated from the surrounding grid points 1-4 using bilinear interpolation. If all these points 1-4 are fluid points with flag 0, it is assumed that any variable in the 2D space can be written in the following form

$$u=a_1+a_2x+a_3y+a_4xy. \tag{3.7}$$

So the standard bilinear interpolation coefficients can be computed as follows

$$\begin{bmatrix} a_1 \\ a_2 \\ a_3 \\ a_4 \end{bmatrix} = \begin{bmatrix} 1 & x_1 & y_1 & x_1y_1 \\ 1 & x_2 & y_2 & x_2y_2 \\ 1 & x_3 & y_3 & x_3y_3 \\ 1 & x_4 & y_4 & x_4y_4 \end{bmatrix}^{-1} \begin{bmatrix} u_1 \\ u_2 \\ u_3 \\ u_4 \end{bmatrix}, \tag{3.8}$$

where (x_1,y_1), (x_2,y_2), (x_3,y_3), and (x_4,y_4) are coordinates of the four points in the fluid. u_v is the virtual point interpolated from the coefficients a_1, a_2, a_3 and a_4 and its coordinate $(x_v,\ y_v)$. u_b is the perpendicular point and also boundary point. Thus the value of any variable u_f at the forcing point is given as

$$u_f=\frac{d_1+d_2}{d_2}u_b-\frac{d_1}{d_2}u_v. \tag{3.9}$$

3.4 Hydrodynamic force calculation on the immersed interface

The force **f** per unit area on a surface element with an outward normal **n** can be written as (Yang et al. 2006)

$$f_i=\tau_{ji}n_j=\left[-p\delta_{ij}+\mu\left(\frac{\partial u_i}{\partial x_j}+\frac{\partial u_j}{\partial x_i}\right)\right]n_j, \tag{3.10}$$

where f_i is the surface force in x_i direction, τ_{ji} is stress tensor and n_j is the direction cosine of **n** in x_j direction. $\partial u_i/\partial x_j$ can be computed using the stencil and interpolation coefficients that were used to construct the velocity field near the interface. Due to grid staggering the derivatives for each velocity are computed on different points on the interface.

Pressure boundary conditions $\partial p/\partial n=0$ are also imposed on the immersed boundary. p needs to be computed on the virtual point thus its value on the body surface is obtained.

3.5 Interaction between body and fluid

In order to ensure numerical stability, a fully fluid-structure coupling method for the body velocity (Kleefsman et al. 2005) is taken as follows. The sub-iterative index m is introduced in the following equation.

$$\left(V_{body}^{k+1}\right)^{m+1}=(1-\alpha)\left(V_{body}^{k+1}\right)^{m}+\alpha\left(V_{body}^{k}+\frac{F_{body}^{m}}{m_{body}}\Delta t\right), \tag{3.11}$$

where Δt is the physical time step; F_{body}^{m} is the hydrodynamic force on the body computed by integration of the pressure and viscous force over the boundary of the moving body; m_{body} is the mass of the body; α is a relaxation factor used to prevent divergence of the sub-iteration process which is in the range from 0 to 1; V_{body}^{k} is the vertical body velocity at the physical time k. At the physical time step k, the iterative initial value $(V_{body}^{k+1})^0$ is taken as V_{body}^{k}. For the sub-iteration a new pressure field is computed based on the vertical velocity $(V_{body}^{k+1})^m$ and the hydrodynamic force is obtained by integration of the new pressure and viscous forces over the body surface. When the residual of the Poisson pressure equation is less than 10^{-6}, the sub-iteration is ended.

4 Results

4.1 Uniform flow past a circular cylinder

Flow over a fixed circular cylinder is simulated to verify that the present immersed boundary method accurately predicts flow phenomena such as separation and vortex. The size of the computational domain is $20d\times 50d$ where d is the cylinder diameter. This is large enough to minimize the effect of the outer boundary on the development of the wake. The computation is performed at a Reynolds number, $\mathrm{Re}=\rho u_\infty d/\mu=100$. A grid size of $\Delta x=\Delta y=0.01d$ with a time step 0.001 is used. Additionally no slip boundary conditions are used on the cylinder with free boundary conditions applied on the right hand, top and bottom walls and a steady unidirectional inlet velocity $u=u_\infty$, $v=0$ applied on the left hand wall. Fig. 3 shows the time history of lift and drag coefficients. The drag coefficient $\mathrm{C_D}$ and lift coefficient $\mathrm{C_L}$ are computed from

$$\mathrm{C_D}=\frac{F_x}{1/2\rho u_\infty^2 d},\qquad \mathrm{C_L}=\frac{F_y}{1/2\rho u_\infty^2 d}, \tag{4.1}$$

where F_x and F_y denote the streamwise and normal hydrodynamic forces around the cylinder in Cartesian coordinates and can be obtained by integrating the pressure and

Table 1: Comparison of drag coefficient, rms of lift coefficient and Strouhal number with previous studies.

	Re = 100		
	$St = fd/u_\infty$	C_D(avg)	C_L(rms)
Current study	0.168	1.41	0.33
Tseng et al. (2003)	0.164	1.42	0.29
Kim et al. (2001)	0.165	1.33	
Dias and Majumdar (2001)	0.171	1.395	0.283
Williamson (Exp.) (1988)	0.166		

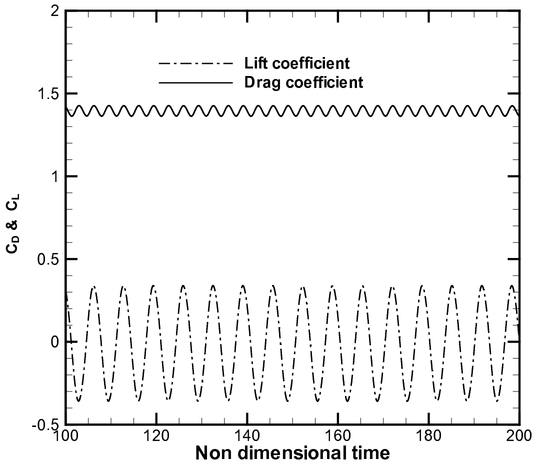

Figure 3: Time history of lift and drag coefficients for uniform flow past a cylinder at Re = 100.

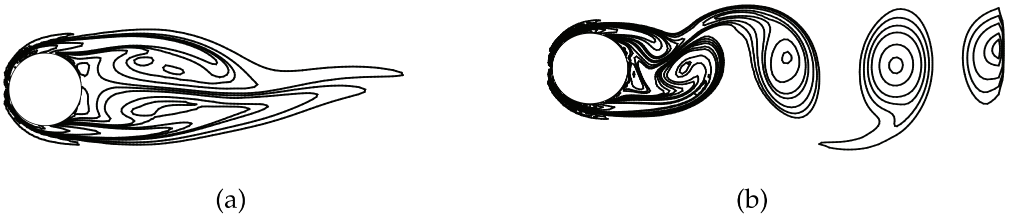
(a) (b)

Figure 4: The instantaneous vorticity contours in the near wake of a cylinder in a uniform flow for Re = 100 in a uniform flow at (a) $T = 25$; (b) $T = 68$.

viscous forces around the cylinder surface using Eq. (3.10). The mean drag coefficient is predicted to be $C_D(\text{avg}) = 1.41$, the rms value of lift coefficient to be $C_L(\text{rms}) = 0.33$ and Strouhal number ($St = fd/u_\infty$, where f is the frequency of vortex shedding) to be $St = 0.168$, all of which agree well with computational results from the literature summarized in Table 1. Fig. 4 shows the spanwise vorticity contours for Re=100 at different nondimensional time instants, where $T = tu_\infty/d$. The Karman vortex street predicted indicates that the vorticity field is well captured by the present immersed boundary method.

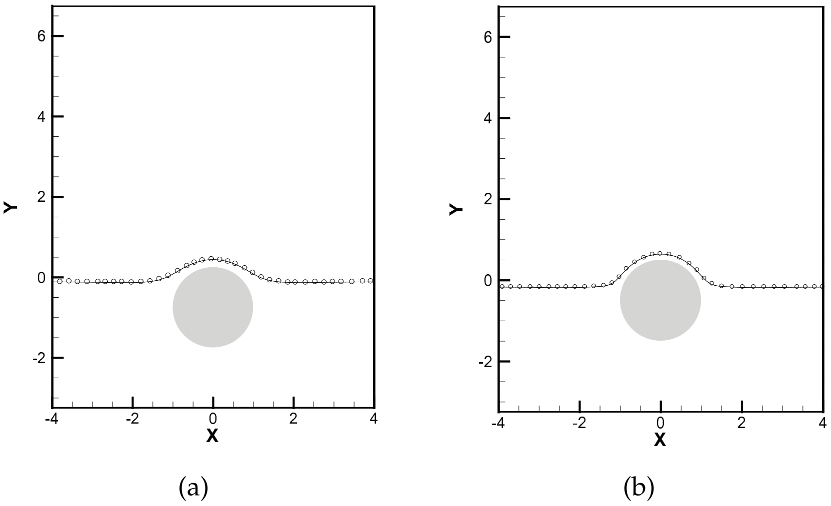

(a) (b)

Figure 5: Comparisons of free surface profiles between the present method (solid black line) and boundary element simulation by Greenhow et al., (1997) (circles) at two non-dimensional time instants (a) $T=0.4$; (b) $T=0.6$.

4.2 Water entry and exit of a cylinder

The problem of water exit of a cylinder is very significant in various practical applications. Understanding such complicated physical processes, including breaking up of the free surface, body-fluid interaction and free surface-vortex interaction, is useful in, for example, understanding the impacts of wave energy converters under extreme waves. This is a severe test for the numerical procedure since the initial impact is considerable and the local deadrise angle is very small thus making the simulation of the penetration processes extremely challenging. Greenhow et al. (1983) conducted experiments of water exit and entry of a horizontal circular cylinder to show the difference of free surface deformation between the entry and exit processes. Greenhow et al. (1997) simulated the processes by using a nonlinear two-dimensional BEM based on the assumption of irrotational flow. Battistin et al. (2003) investigated the hydrodynamic loads during water entry of axisymmetric bodies using the boundary element formulation based on potential flow. Kleefsman et al. (2005) applied the VOF with a local height function to solve the water entry problem. Lin (2007) used a VOF one phase model and cut-cell technique in a fixed grid system to simulate the water entry and exit.

A cylinder of $r=1$m is placed in calm water in a rectangular tank of width $=8$m, height $=10$m and the distance of its centre to the free surface $d=1.25$m. The time step Δt=0.0001s is used for the simulation of water entry and exit. The water has dynamic viscosity 1×10^{-3}kg/m/s and the air 1.8×10^{-5}kg/m/s, the density of water is 1000kg/m^3 and air 1kg/m^3. The cylinder is given a constant upward velocity, $V=0.39$m/s. Thus the dimensionless parameters are $\varepsilon=r/d=0.8$, $F_r=V/\sqrt{gr}=0.39$ and $T=Vt/d$. The comparison of free surface profiles between the present numerical method and those presented by Greenhow et al. (1997) is shown in Fig. 5 at two non-dimensional time instants, $T=0.4$ and 0.6. Good agreement can be seen.

Snapshots of the interaction between the cylinder and interface are shown in Fig. 6 at exit velocity $V=0.39\text{m/s}$. As the cylinder moves upward, the cylinder deforms the free surface and waves are generated in the exit process and propagate towards both sides of the cylinder. Breaking can occur during exit due to strongly negative pressures arising on the cylinder surface.

Here, the same parameters as used in the water exit of a cylinder problem are used. The cylinder starts its downward motion from a height of $d=1.25\text{m}$ to the calm water surface with a constant velocity $V=-1\text{m/s}$. Snapshots of two different instants in time are shown in Fig. 7 and are compared with photographs of experiments by Greenhow et al. (1983). The free surface observed in the experiment is captured very well by our model. And a series of snapshots is shown in Fig. 8. When the cylinder moves close to the free surface at $T=0.2$, the small air gap between the free surface and body surface is very important and causes the free surface to deform. As the cylinder impinges on the free surface at $T=0.6$, there are jets generated on both sides of the cylinder. When the cylinder moves further downward, a large amount of water is pulled downward and the surface depression persists at $T=2.0$. As the cylinder is fully submerged in the water at $T=4.0$, there is a water jet in the centre of the water surface. The results are very close to those reported by Lin (2007). The water jets are captured very well by the two phase model.

The slamming coefficient is given by

$$C=\frac{F}{\rho r V^2}, \tag{4.2}$$

where F is the total vertical hydrodynamic force, r is the radius of the cylinder and V is the entry velocity. Based on potential flow theory, the hydrodynamic slamming force is given by

$$F=\frac{\pi}{2}\rho V\left(2Vr-2V^2t\right), \tag{4.3}$$

where t is the time at the moment of the first impact. Fig. 9 shows comparison of the slamming coefficient versus the penetration depth for present model results with theoretical results of Von Karman, (1929), experimental results of Campbell and Weynberg (1980) and numerical results using ComFlow (Kleefsman et al. 2005). The comparison is reasonably good. At the beginning, an impulsive high pressure is generated and the initial slamming coefficient reaches 4.0. Later the cylinder is submerged in the water and experiences a buoyancy force and the slamming coefficient is around 1.6. The slamming coefficient predicted by the presented model does not reach the initial peak value measured in the experiment, but the variation in slamming coefficient with penetration depth agrees better in the later stages of the impact with the experiment. The slamming coefficient oscillates along the penetration depth at the initial impacting stages, which is due to the lack of stability of the pressure distribution near the body boundary in this method.

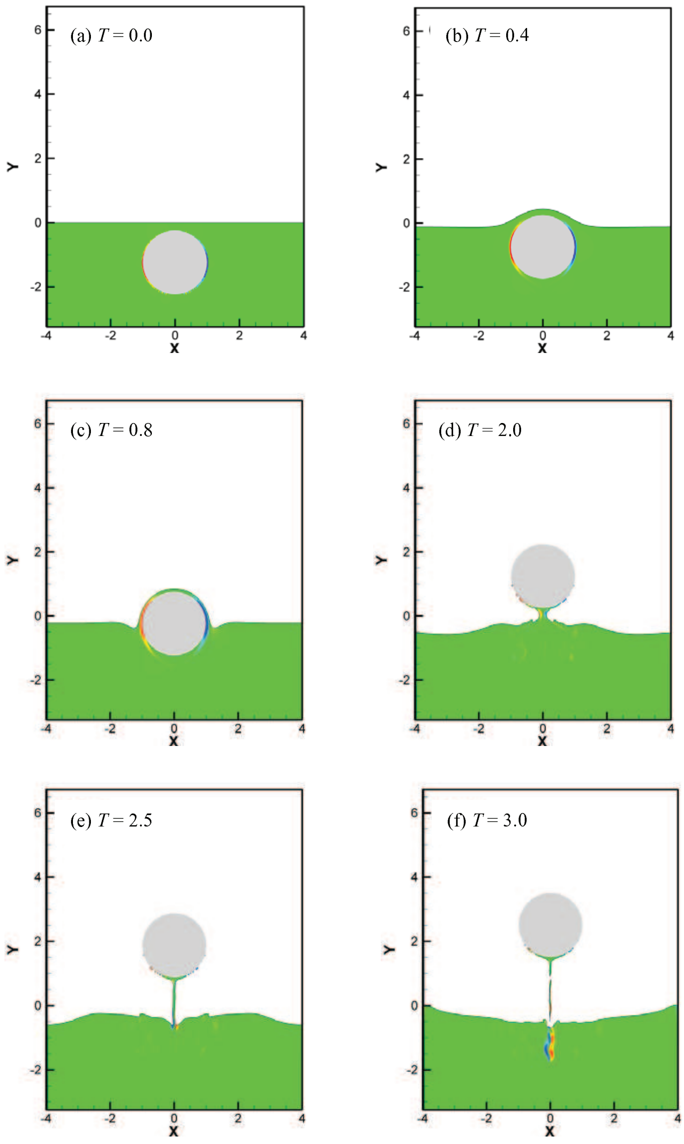

Figure 6: Water exit of a cylinder at $V = 0.39$m/s. The free surface position (solid black line) and vorticity strength (shading, $-10 \sim 10$ with intervals 0.2) at non-dimensional time (a) $T = 0$; (b) $T = 0.4$; (c) $T = 0.8$; (d) $T = 2.0$; (e) $T = 2.5$; (f) $T = 3.0$.

4.3 Free falling of the wedge

As the velocity of a wedge during a free fall into a liquid depends on the interaction between the wedge and the surrounding fluid, it is a big challenge for most models to treat the free surface and moving solid bodies together. The immersed boundary coupled

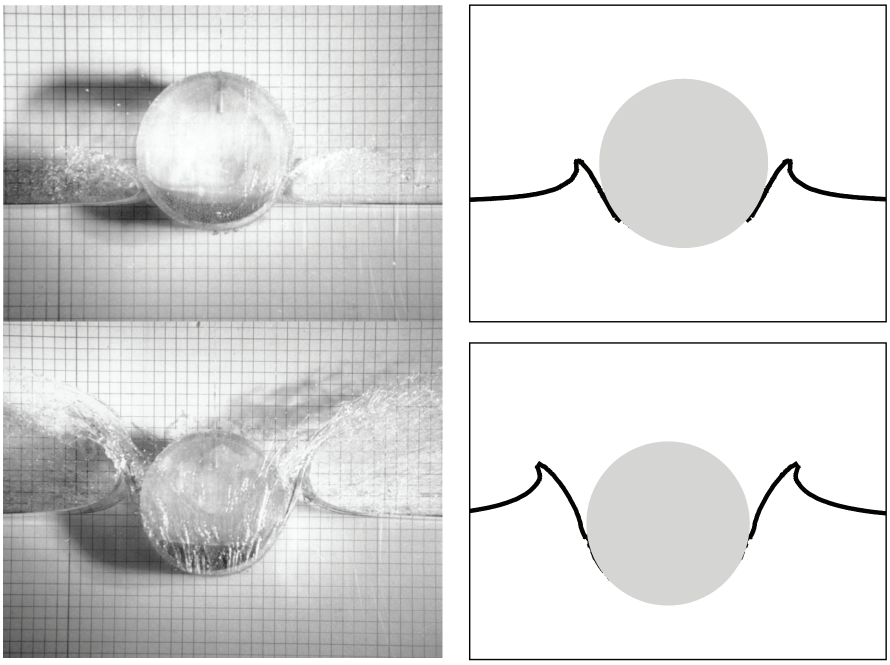

Figure 7: Comparisons of simulated water entry of a cylinder (right panels) and experiment (left panels, Greenhow et al., (1983)).

level set model with global mass correction is used to simulate the water entry of a free falling wedge and results compared with the experimental and numerical work of Zhao et al. (1997), Kleefsman et al. (2005) and Oger et al. (2006) and Shao (2009). The wedge section used in the experiment by Zhao et al. (1997) is shown in Fig. 10. The breadth of the wedge is 500mm. The V-shaped section has a 30° dead-rise angle. The total weight of the drop rig is 241kg and a ballast weight of 100kg. The vertical motion is the only degree of freedom for the wedge in this experiment. A detailed description of the experiment can be found in Zhao et al. (1997). The numerical simulation is based on the above experiment to calculate the water entry of a free falling wedge. The numerical tank is 2m wide and 1m deep. The water has dynamic viscosity 1×10^{-3}kg/m/s and the air 1.8×10^{-5}kg/m/s, the density of water is 1000kg/m^3 and air 1kg/m^3, and the acceleration due to gravity is taken to be $g=9.81$m/s^2. The initial conditions were defined using the exact velocity $V=-6.15$m/s.

Fig. 11 shows the grid convergence tests for a free falling wedge. Grid sizes of $\Delta x=\Delta y$=0.01m with a time step Δt=10^{-4}s, Δx=Δy=0.005m with a time step Δt=5×10^{-5}s and $\Delta x=\Delta y=0.0025$m with a time step $\Delta t=2.5\times10^{-5}$s respectively are used to simulate the free falling wedge and results compared with those of Zhao et al. (1997). Grid refinement for free surface profiles is shown in Fig. 11(a). The finer the grid, the better the jets are captured. Also the free falling velocity and vertical slamming force agree much better

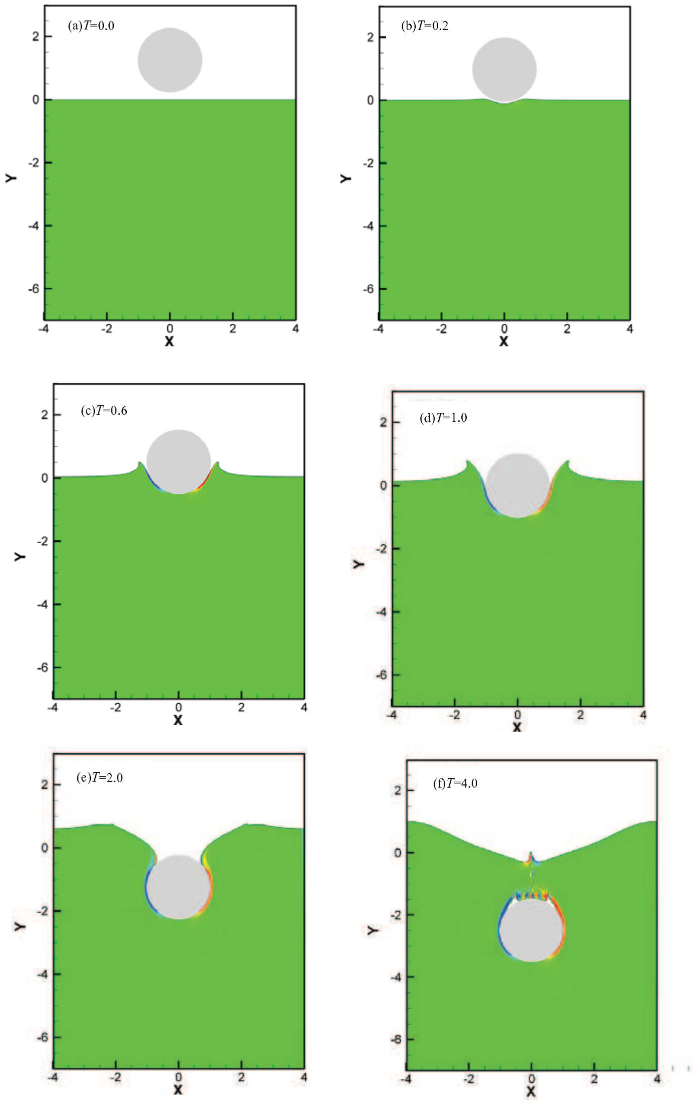

Figure 8: Water entry of a cylinder at $V=-1.0$m/s. The free surface position (solid black line) and vorticity strength (shading, $-10\sim10$ with intervals 0.2) at non-dimensional time (a) $T=0$; (b) $T=0.2$; (c) $T=0.6$; (d) $T=1.0$; (e) $T=2.0$; (f) $T=4.0$.

with Zhao et al. (1997) for the fine grid. Fig. 12 presents the comparison of snapshots between the experimental photographs (Greenhow et al. 1983) and present model of $\Delta x=\Delta y=0.0025$ for the free falling wedge entry with deadrise angle 30°. The visual comparison is very good.

When the water entry of a free falling wedge is simulated using the immersed boundary method, the slow convergence of the Poisson pressure equation is exacerbated. Use

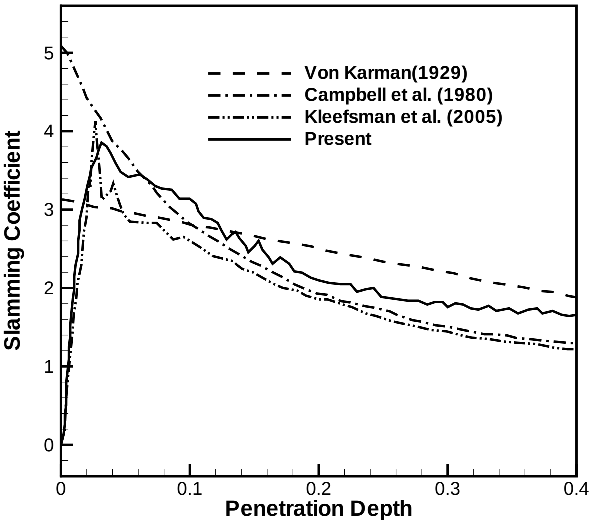

Figure 9: Comparisons of slamming coefficients between present model, the theory of Von Karman (1929), experimental data of Campbell et al. (1980), numerical simulation of Kleefsman et al. (2005).

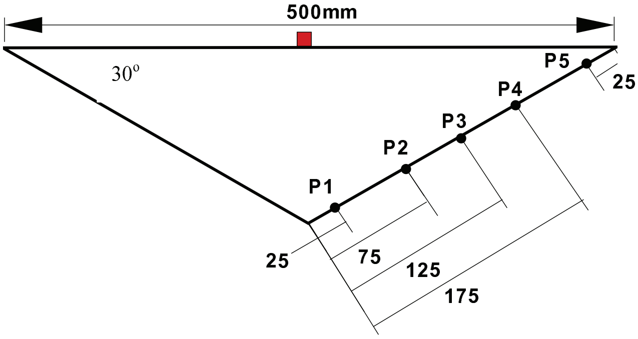

Figure 10: Wedge section used in the experiment and pressure gauge locations P1-P5.

of GMRES with incomplete LU factorization for preconditioning is found to speed up the computation and accelerates the convergence significantly with less sub-iteration numbers. This is shown in Fig. 13, where the convergence rates of GMRES and TDMA (TriDiagonal-Matrix Algorithm, (Patankar 1980)) are compared.

Fig. 14 shows the calculated pressure field and the pressure comparison at different instants near the wedge boundary. The figures in the left panels give a clear and visual explanation of the pressure curves obtained. Fig. 14(b) highlights the pressure peak in the area of pressure cell P5. Fig. 14(c) gives the pressure peak in the area of pressure cell P1. The pressure from the present simulation is underestimated for the instant $t=0.00435$s when compared with both the experimental and numerical results of Zhao et al. (1997). At the very beginning of the impact, the wedge impinging the free surface leads to sud-

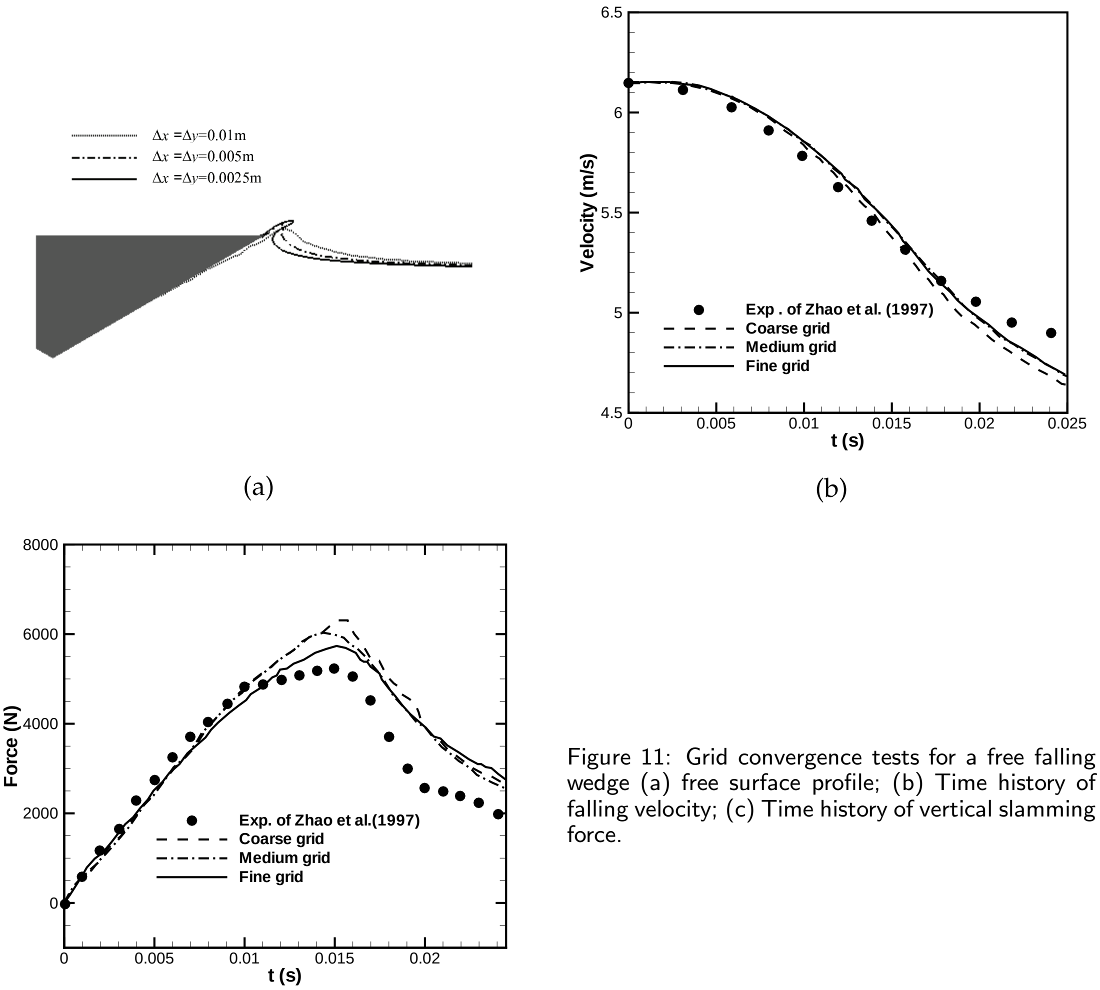

(a) (b)

(c)

Figure 11: Grid convergence tests for a free falling wedge (a) free surface profile; (b) Time history of falling velocity; (c) Time history of vertical slamming force.

den and excessive change of the pressure in the fluid. Furthermore the gas phase does not develop well at the very beginning and the instability between the gas and liquid influences the instantaneous pressure capture. For $t = 0.0158$s, this underestimation still exists but becomes smaller compared with the instant $t = 0.00435$s. At this time, the pressure coefficient agrees with the experimental data better than the numerical simulation of Zhao et al. (1997). However, the maximum pressure coefficient is far lower than either the experimental data or numerical simulation of Zhao et al. (1997). At $t = 0.0202$s, the present results overpredict compared with the experiment. This is possibly due to the three-dimensional effects, as mentioned by Zhao et al. (1997).

To quantitatively demonstrate the accuracy of the immersed boundary level set with the global mass correction, the falling velocity of the wedge and the fluid forces acting on the wedge are shown in Figs. 15(a) and (b). Fig. 15(a) shows the vertical fluid forces acting

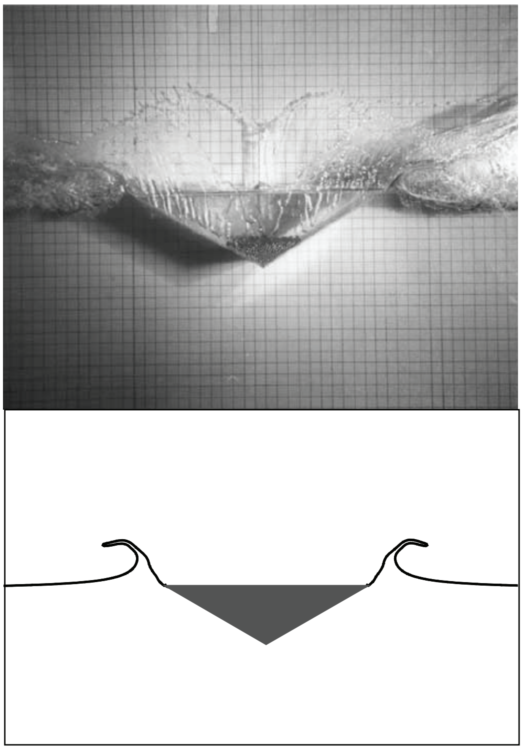

Figure 12: Free surface profile of free falling wedge with deadrise angle 30° (Bottom: present model; Top, Experiment by Greenhow et al., (1983)).

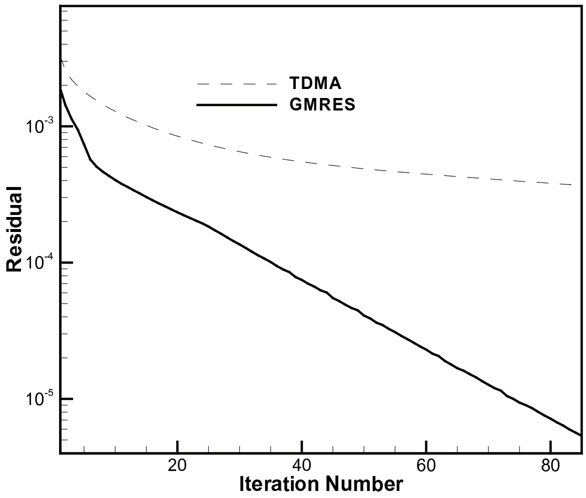

Figure 13: Comparison of convergence rates of TDMA and GMRES applied to the Poisson pressure equation for the free falling wedge.

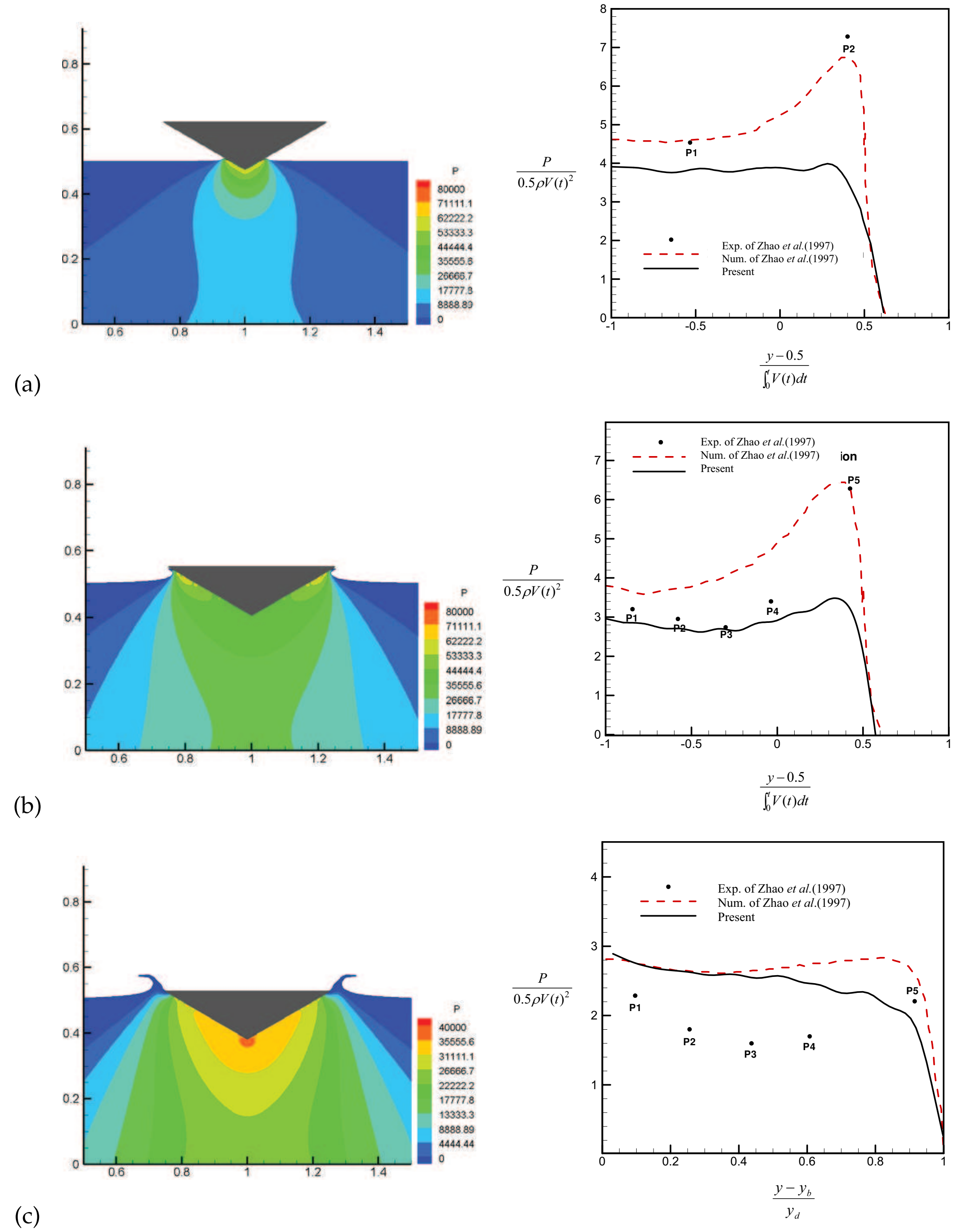

Figure 14: Calculated pressure distribution(left panels) and comparisons of pressure at the wedge boundary (right panels) for different instants: (a) $t=0.00435$ s; (b) $t=0.0158$ s; (c) $t=0.0202$ s. P is the pressure, $V(t)$ denotes wedge vertical velocity at that time instant, y is vertical coordinate on the wedge surface, y_b is the vertical coordinate of the keel and y_d is the draft of the body.

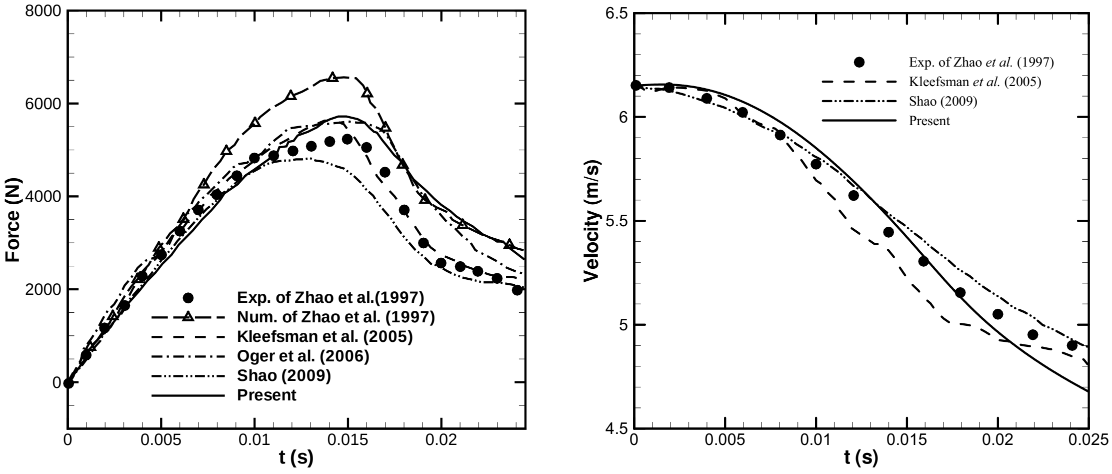

(a) (b)

Figure 15: (a) Time history vertical slamming forces. (b) Time history falling velocity.

on the falling wedge. It is seen that there are two stages for the change of the vertical force. In the first stage ($0\text{s} < t < 0.016\text{s}$) high pressure is generated at the initial impact which leads to an increase in the vertical hydrodynamic force on the wedge. In the second stage ($0.016\text{s} < t < 0.025\text{s}$), the wedge is fully wetted. This causes a drop of the vertical force. All the numerical results agree well with the experiment data before $t = 0.0125\text{s}$. After $t = 0.015\text{s}$, Shao, 2009 underestimates the force and Kleefsman et al. (2005) accurately predicts the force while Zhao et al. (1997), Oger et al. (2006) and the present method overpredict the peak force. This overpredicted force after $t = 0.015\text{s}$ generates stronger deceleration than the experiment and results in the slow motion of the wedge falling into the water compared to the experiment as shown in Fig. 15(b).

5 Conclusions

The new level set immersed boundary method has proven to be a valuable tool for investigating complex cases of fluid-structure interaction and wave impacts. The incorporation of an improved immersed boundary method with the free surface flow allows a curved body to be modelled easily and enables the various applications of fluid structure interaction to be tackled. In this paper, a new method to classify the grid points and locate the forcing points was presented. The momentum forcing was imposed by introducing ghost node inside the boundary resulting in ease of grid generation. GMRES was applied to accelerate the convergence of the Poisson pressure equation.

This method was validated using uniform flow past a circular cylinder. Predicted lift coefficient, drag coefficient and Strouhal number for uniform flow past a cylinder at Reynolds number 100 agree well with the experimental data and computational results from the literature. More detailed free surface evolutions and wave generations were seen in snapshots of the water-air interface contours and vorticity strength for water exit and entry of a cylinder. The visual agreement between snapshots of the simulations and photographs of experiments by Greenhow et al. (1983) is very good. The slamming coefficient predicted by the present model for the water entry of a cylinder at the prescribed velocity shows a fair agreement with the experimental data by Campbell et al. (1980) and previous numerical simulations using ComFlow (Kleefsman et al. 2005). Finally, for the free falling wedge, a full coupling between fluid and body movement was investigated. The vertical slamming force predicted by the present model agrees well with the experiment at the early stages. Later, the model overestimates the peak force causing a stronger deceleration and slower motion of the wedge because it does not account for the three-dimensional effects.

The present method is currently being extended to simulate the coupled dynamic response of the wave energy converter and mooring system under extreme wave loading. The dynamic response of the mooring lines is strongly coupled with the hydrodynamic motion of the wave energy converter and may affect its performance.

Acknowledgments

The authors gratefully acknowledge the support of the South West of England Regional Development Agency in funding this project through Peninsular Research Institute for Marine Renewable Energy (http://www.primare.org/). The authors also would like to acknowledge the support of the Natural Environmental Research Council (Grant No. NE /E002129/1) during this project.

References

[1] Balaras E., 2004. Modeling complex boundaries using an external force field on fixed Cartesian grids in large-eddy simulations. Computers and Fluids 33, 375-404.
[2] Battistin D., Iafrati A., 2003. Hydrodynamic loads during water entry of two-dimensional and axisymmetric bodies. Journal of Fluids and Structures 17, 643-664.
[3] Baum J.D., Luo H., Lohner R., Yang C., Pelessone D. and Charman C., 1996. A coupled Fluid/Structure modelling of shock interaction with a truck. AIAA, 0795.
[4] Campbell I.M.C. and Weynberg P.A., 1980. Measurement of parameters affecting slamming. Report No. 440,Wolfson Unit of Marine Technology, Tech. Rep. Centre No. TO-R-8042, Southampton.
[5] Chang Y.C., Hou T.Y., Merriman B., Osher S., 1996. A Level Set Formulation of Eulerian Interface Capturing Methods for Incompressible Fluid Flows. Journal of Computational Physics 124, 449-464.
[6] Dias A., Majumdar S., 2001. Numerical computation of flow around a circular cylinder, Technical Report, PS II Report, BITS Pilani, India.

[7] Fadlun E.A., Verzicco R., Orlandi P., Mohd-Yusof J., 2000. Combined immersed-boundary finite-difference methods for three-dimensional complex flow simulations. Journal of Computational Physics 61, 35-60.

[8] Ferziger J.H. and Peric M., 2002. Computational Methods for Fluid Dynamics (3rd edn). Springer: New York.

[9] Goldstein D., Handler R. and Siirovich L., 1993. Modeling a no-slip flow boundary with an external force field. Journal of Computational Physics 105, 354-366.

[10] Greenhow M. and Lin W., 1983. Non-linear free surface effects: experiments and theory. Report Number 83-19, Department of Ocean Engineering, Massachusetts Institute of Technology.

[11] Greenhow M. and Moyo S., 1997. Water entry and exit of horizontal circular cylinders. Philosophical Transactions of Royal Society A 355(1724), 551-63.

[12] Kim J., Kim D., Choi H., 2001. An immersed-boundary finite-volume method for simulations of flow in complex geometries. Journal of Computational Physics 171, 132-150.

[13] Kleefsman K.M.T., Fekken G., Veldman A.E.P., Iwanowski B. and Buchner B., 2005. A volume-of-fluid based simulation method for wave impact problems. Journal of Computational Physics 206, 363-393.

[14] Lin P.Z., 2007. A fixed grid model for simulation of a moving body in free surface flows. Computers and Fluids 36, 549-561.

[15] Lv X., Zhao Y., Huang X.Y., Xia, G.H. and Wang Z.J., 2006 An efficient parallel/unstructured-multigrid preconditioned implicit method for simulating 3D unsteady compressible flows with moving objects. Journal of Computational Physics 215, 661-690.

[16] Mittal R. and Iaccarino G., 2005. Immersed boundary methods. Annual Review of Fluid Mechanics 37, 239-261.

[17] Oger G., Doring M., Alessandrini B., Ferrant P., 2006. Two-dimensional SPH simulations of wedge water entries. Journal of Computational Physics 213, 803-822.

[18] Patankar S. V., 1980. Numerical Heat Transfer and Fluid Flow. Hemisphere/Mcgraw hill: Washington.

[19] Shao S. D., 2009. Incompressible SPH simulation of water entry of a free-falling object. International Journal for Numerical Methods in Fluids 59, 91-115.

[20] Sussman M., Smereka P., Osher S., 1994. A Level Set Approach for Computing Solutions to Incompressible Two-Phase Flow. Journal of Computational Physics 114, 146-159.

[21] Tucker P. and Pan Z., 2000. A Cartesian cut cell method for incompressible viscous flow. Applied Mathematical Modelling 24, 591-606.

[22] Tseng Y.H., Ferziger J. H., 2003. A ghost-cell immersed boundary method for flow in complex geometry. Journal of Computational Physics 192, 593-623.

[23] Von Karman T., 1929. the impact of seaplane floats during landing. NACA Technical Note, vol. 321. Wahsington, DC:NACA.

[24] Wang, Z. Y., Zou Q. P. and Reeve D. E., 2009. Simulation of spilling breaking waves using a two phase flow CFD model, Computers & Fluids 38 (10), 1995-2005.

[25] Waterson N.P. and Deconinck H.. Desigh principles for bounded higher-order convection schemes- a unified approach. Journal of Computational Physics 2007; 224:182-207.

[26] Williamson C. H. K. and Roshko A., 1988. Vortex formation in the wake of an oscillating cylinder. Journal of Fluids and Structures 2, 355-381.

[27] Yan S. and Ma Q.W., 2007. Numerical simulation of fully nonlinear interaction between steep waves and 2D floating bodies using the QALE-FEM method. Journal of Computational Physics 221, 666-692.

[28] Yang G., Causon D., Ingram D., Saunders R., Batten P., 1997. A Cartesian cut cell method for compressible flows. Part A. Static body problems. Aeronautical Journal 101 (1001), 47-56.

[29] Yang J.M. and Balaras. E., 2006. An embedded-boundary formulation for large-eddy simulation of turbulent flows interaction with moving boundaries. Journal of Computational Physics 215, 12-40.

[30] Yap Y.F., Chai J.C., Wong T.N., Toh K.C., Zhang H.Y., 2006. A global mass correction scheme for the level set method. Numerical Heat Transfer, Part B 50,455-472.

[31] Ye T., Mittal R., Udaykumar H., Shyy W., 1999. An accurate Cartesian grid method for viscous incompressible flows with complex immersed boundaries. Journal of Computational Physics 156, 209-240.

[32] Yousef S. and Martin H.S., 1986. GMRES: a generalized minimal residual algorithm for solving nonsymmetric linear systems. SIAM Journal of Scientific and Statistical Computing 7 (3), 856-869.

[33] Zhang Y.L., Zou Q.P., Greaves D., 2010. Numerical simulation of free surface flow using the level set method with global mass correction. International Journal for Numerical Methods in Fluids, DOI: 10.1002/fld.2090.

[34] Zhao R., Faltinsen O., Aarsnes J., 1997. Water entry of arbitrary two-dimensional sections with and without flow separation, in: 21st Symposium on Naval Hydrodynamics.